SCIEPublish

Article

Energy Harness and Wake Structure of "Cir-Tri-Att" Oscillators for Flow-Induced Motion Tidal Energy Conversion System

Xu Yang [1,2], Liuyang Jiang [1], Ye Yao [1,2], Xifeng Gao [1,2,*], Xiang Yan [2,3], Nan Shao [4] and Jiale Xiang [2,3]

[1] Institute of Ocean Energy and Intelligent Construction, Tianjin University of Technology, Tianjin 300384, China; yangxuyx1990@163.com (X.Y.); jly200929@163.com (L.J.); yaoye-111@163.com (Y.Y.)

[2] State Key Laboratory of Hydraulic Engineering Intelligent Construction and Operation, Tianjin University, 135 Yaguan Road, Jinnan District, Tianjin 300072, China; xiangyan@tju.edu.cn (X.Y.); 1461228613@qq.com (J.X.)

[3] School of Civil Engineering, Tianjin University, 135 Yaguan Road, Jinnan District, Tianjin 300072, China

[4] School of Water Conservancy and Hydroelectric Power, Hebei University of Engineering, Handan 056038 China; shaonan89@126.com (N.S.)

* Corresponding author. E-mail: gaoxifeng@tju.edu.cn (X.G.)

Received: 21 January 2025; Accepted: 20 February 2025; Available online: 25 February 2025

ABSTRACT: The research focuses on the flow-induced motion (FIM) and energy harness of "Cir-Tri-Att" oscillators (CTAO). The wake was photographed by particle image velocimetry (PIV) to explore wake structures. With the increase of the aspect ratios: the ability of oscillators to galloping under self-excitation or external excitation is enhanced. When ζ = 0.033, U_r = 12.5, the maximum amplitude ratio A^* = 2.408 for oscillators with α = 1:1. Moreover, oscillators with higher aspect ratios can bear larger loads, which is conducive to energy utilization and conversion. The maximum power output P_{harn} = 16.588 W and the optimal efficiency η_{harn} = 24.706% appear in oscillators with α = 1.5:1. Additionally, In the soft galloping (SG), the wake mode is 4P or 3P. The wake vortex is more broken and its scale increases, but the force effect of the oscillators is better and the oscillation is more stable. The pressure difference makes for a longer oscillation period. This paper summarizes the FIM, energy harness and wake structures of the CTAO under different working conditions, which provides theoretical and data support for the optimization oscillators of flow-induced motion tidal energy conversion system.

Keywords: Tidal energy; Flow-induced motion; Energy harness; Wake structures

1. Introduction

In the face of growing demand for energy and sustainable development requirements, high-quality clean energy has become one of the main directions of energy structure reform in various countries [1–3]. Marine energy, with its vast untapped resource potential, provides important support for the realization of the "dual carbon" goals [4] and receives much attention in academic research.

As a kind of marine energy, tidal energy has significant development value because of its abundant resources [5], stable and predictable characteristics [6]. Tidal energy can be generated by a variety of technologies, including barrages type, axial flow type, vertical type and reciprocating type. At present, the most common tidal energy device is the horizontal axis turbine. However, its initial starting flow velocity is high, and its application in many low-flow velocity areas is limited [7,8]. Therefore, it is very important to develop an effective capture tidal energy device at low flow velocity.

FIM is divided into vortex-induced vibration (VIV) and galloping. It is generally caused by vortex shedding or dynamic instability when the fluid flows through the bluff body structures [9–11]. When the amplitude of these oscillations reaches a certain threshold, they will cause damage to the engineering structure, bringing safety hazards and economic losses. Therefore, a large number of scholars focus on how to suppress the FIM [12,13].

With the development of marine energy technology, research in recent years has begun to reconsider FIM from the perspective of energy harness [14–16]. Bernitsas proposed a vortex-induced vibrations for aquatic clean energy (VIVACE) device [17,18]. This device has significant advantages, including a low initial starting flow velocity and

https://doi.org/10.70322/mer.2025.10002

high energy density, and achieves a breakthrough in the electromagnetic energy harness of FIM. Based on it, scholars have conducted a series of studies on how to improve energy harness efficiency, which can be roughly categorized into two directions.

One is to improve the cylindrical oscillators: Park and Kumar [19] could effectively change the pressure distribution on the surface of the cylinder by changing the roughness of the cylinder through passive turbulence control. During the experiment, they found two different galloping modes of the cylinder: Soft galloping (SG) and hard galloping (HG). Chen et al. [20] conducted experiments on cylinders with different diameters and found that galloping offers harnessed power that is three times larger than the VIV. Still, the maximum efficiency is in the VIV. Feng et al. [21] verified the experimental setup of flow-induced rotation (FIR) of coupled double cylinders in tandem and established the theoretical basis of FIR.

The other is to explore non-cylindrical oscillators: Zhang et al. [22] explored the FIM of the equilateral triangular prism and found that its oscillation response does not inhibit the increase of the reduced velocity. Yan et al. [23] tested the galloping characteristics of the T-section prism. The experimental results indicate that the soft galloping occurs when the damping ratios are small and oscillators exhibited self-excitation characteristics. Lian et al. [24] conducted FIM experiments on two rigidly coupled triangular prisms in tandem arrangement. The experimental results indicate that the "sharp jump" phenomenon may appear at specific spacing ratios. Ran et al. [25] designed a novel "Cir-Tri-Att" oscillator and carried out experiments on oscillators with an aspect ratio 1:1 in the range of 0–100 V excitation voltages. This oscillator can utilize energy from both the VIV and the galloping. The experimental results indicate that the energy harness capacity of the oscillator is better than that of the triangular prism.

Recently, Liu et al. [26] improved Ran's experiment by expanding the regulation range of excitation voltage to 0-200 V and tested four CTAO with different aspect ratios under certain stiffness. It is worth mentioning that the PIV was introduced into the experiment to capture the wake of typical working conditions.

The Liu's research only analyzed the influence of aspect ratios on the oscillation and wake under specific working conditions. Based on their work, this paper further explored not only the experimental analysis of the influence of the aspect ratios on energy harness, and used PIV to analyze the wake structures. It provided a systematic summary of the FIM, energy harness and wake structures of the CTAO under different working conditions, providing theoretical and data support for the optimal oscillators of flow-induced motion tidal energy conversion system.

2. Numerical Model and Experimental Devices

2.1. Numerical Model

The flow-induced motion tidal energy conversion system consists of an oscillation part, transmission part and energy harness part. It integrates the flow, oscillator, generator and load to simulate a tidal energy device. Additionally, the heating loss of the load is regarded as the active power of a flow-induced motion tidal energy conversion system.

Numerical model in Reference [27]:

(1) The kinematics equation of the system can be expressed as:

$$\left(m_{osc}+m_a\right)\ddot{y}+c_{total}\dot{y}+Ky=F_L \tag{1}$$

where m_{osc} and m_a represent the oscillation mass and additional water mass of the system, respectively; y, $\dot{y}$ and $\ddot{y}$ represent the displacement, velocity and acceleration of oscillation, respectively; c_{total} is the total damping of the system; K is the stiffness； F_L is the incoming fluid force.

(2) The energy harness of the system can be expressed as:

$$P_{harn}=2\pi^2\frac{n^2L^2R_L(Af_{osc})^2}{(R_0+R_L)^2}L_B^2V_B^2 \tag{2}$$

$$\eta_{harn}=\frac{P_{harn}}{P_w}=4\pi^2\frac{n^2L^2R_L(Af_{osc})^2}{\rho U^3Dl(R_0+R_L)^2}L_B^2V_B^2 \tag{3}$$

where P_{harn} is the power output of the system; η_{harn} is the efficiency of the system; P_w is the total power of the fluid.

Among:

$$P_w = \frac{1}{2}\rho U^3 Dl \tag{4}$$

2.2. Experimental Devices

2.2.1. Experimental Layout

The experiment is carried out in the State Key Laboratory of Hydraulic Engineering Intelligent Construction and Operation of Tianjin University. Experimental devices are mainly composed of the following parts:

(1) Recirculating Water Channel

As shown in Figure 1, the experimental part is arranged in a 1 m flow channel, and the experimental water depth is maintained at 1.34 m; the variable frequency power pump can drive the uniform motion of the flow, and the flow velocity can be controlled by the frequency converter. According to the conclusion of the turbulence intensity measured by Shao [28], the turbulence difference within the experimental part is minimal, and the fluid in the experimental part can be generally guaranteed to be uniform flow.

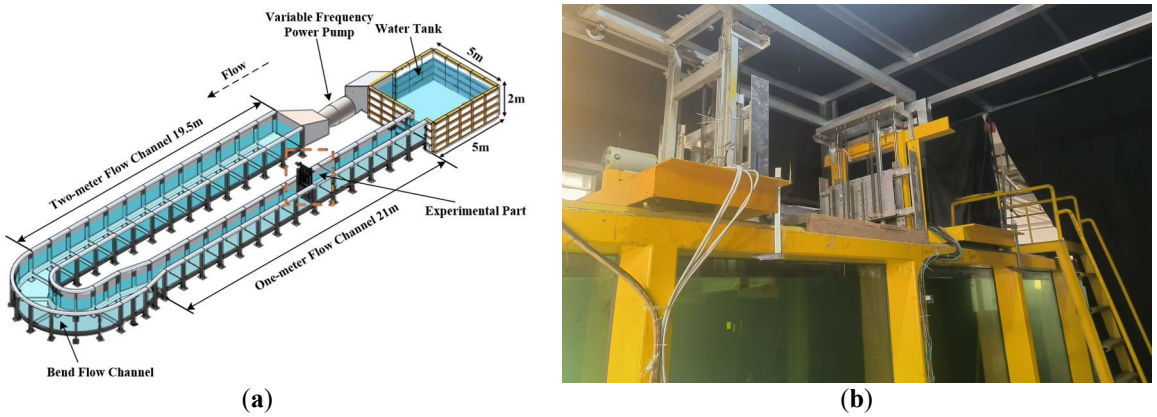

(**a**) (**b**)

Figure 1. Recirculating water channel. (**a**) Overall layout of recirculating water channel schematic; (**b**) Real space of recirculating water channel.

(2) Oscillation and Transmission Part

The oscillator is placed in the water and laterally constrained between side struts, so the oscillator only moves up and down. The linear guideways are fixed on the frame, parallel to the frame and perpendicular to the flow direction. The spring carrier structure is connected to the transmission part and the frame, respectively, so the oscillator can perform a linear reciprocating motion.

(3) Energy Harness Part

The oscillation part is connected to the variable excitation generator through the rack and gears. When the oscillator vibrates, the rack and gears convert the linear reciprocating rotation, which drives the generator rotor to cut magnetic lines to generate electric energy and transmit it to the load resistance to simulate the consumption of tidal energy. The system damping ratios can be changed by a controllable magnetic damping system. The amplitude and frequency are collected by the transducer in real-time and transmitted to the data acquisition & signal processing (DASP) device in the form of electrical signals.

The energy harness part is shown in Figure 2.

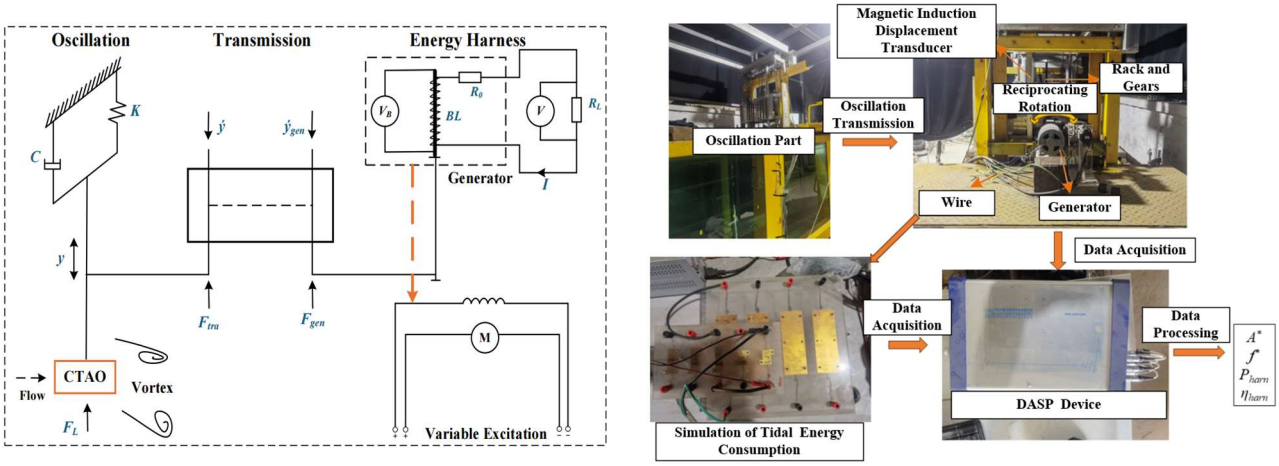

(**a**) (**b**)

Figure 2. The energy harness part. (**a**) Schematic of flow-induced motion tidal energy conversion system; (**b**) Real space of the energy harness part.

(4) PIV System

Table 1 illustrates the components and parameters of the PIV system.

Table 1. Components and parameters of the PIV system.

Components	Parameters
Dual-cavity laser	Dual Power 425-10 PIV Laser, 2 × 425 mJ & 10 Hz, 532 nm
CCD camera	FlowSense EO 16M-9, 4896 × 3264, 8.8 fps
Lens	Nikon 50 mm F/1.8D
Software	Dynamic Studio 5.1
Tracer particles	Hollow Glass Spheres, Diam: 10 μm, 250 g

During the experiment, tracer particles are placed into the experimental part. The laser is refracted through the prism to form a light curtain and captured by the CCD camera. The image data is transmitted to the image processing system in real-time by the synchronizer. The instantaneous velocity can be calculated by the displacement of the tracer particles during the exposure time, as the real state of the flow field can be obtained.

(5) Oscillators

In this experiment, the CTAO is selected, and its section consists of a partial circle, a large triangle and two smaller triangles. Plexiglass end-plates with a thickness of 0.01 m are added to both ends of the oscillator to weaken the influence of boundary conditions on oscillation. The attached plate, also 0.01 m, is positioned at a circumferential angle of 60°. Additionally, the oscillator is designed with a hollow interior to facilitate weight adjustment, and four different aspect ratios are tested: α = 1:1, α = 1.25:1, α = 1.5:1, α = 1.75:1. The configuration is shown in Figure 3.

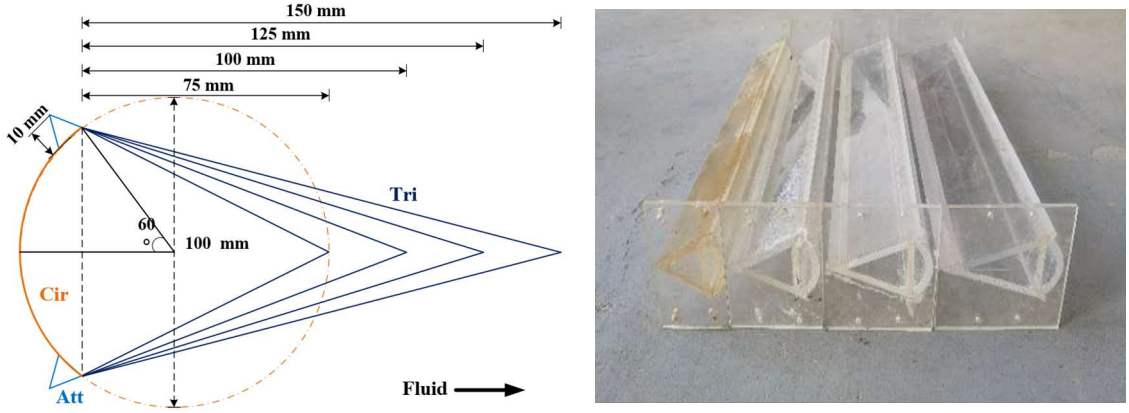

(**a**) (**b**)

Figure 3. The "Cir-Tri-Att" oscillator. (**a**) Section of the "Cir-Tri-Att" oscillator; (**b**) Physical model of the "Cir-Tri-Att" oscillator.

2.2.2. Verification

In this experiment, the system damping ratio needs to be adjusted, that is, the excitation voltage needs to be changed. Therefore, it is necessary to determine whether the system mass remains constant under different excitation voltages and to verify whether the relationship between the total damping and the excitation voltage in the numerical model matches the experimental devices. Considering the special configuration of CTAO, the free decay test under different excitation voltages is carried out in the air [28,29]. The oscillation mass, total damping and system damping ratio are calculated by the following equations:

$$f_n = \frac{1}{2\pi}\sqrt{\frac{K}{m_{osc}}} \tag{5}$$

$$\zeta = \frac{\ln \eta}{2\pi} = \frac{1}{2\pi}\ln\frac{A_i}{A_{i+1}} \tag{6}$$

$$c_{total} = 2\sqrt{m_{osc}K}\cdot\zeta \tag{7}$$

where f_n is the natural frequency of the system; ζ is the system damping ratio; mosc is the oscillation mass of the system; A_i is the amplitude of the ith peak; A_{i+1} is the amplitude of the i+1th peak.

The CTAO of each working condition is carried out four free decay tests. And in the case of reasonable error, the average of the four tests is taken. The results are shown in Table 2.

Table 2. Free decay test results under different excitation voltages.

V_B/V	f_n/Hz	m_{osc}/kg	ζ	c_{total}/(N·s·m^{-1})
0	0.976	31.931	0.033	12.793
10	0.976	31.931	0.036	13.932
20	0.976	31.931	0.041	16.213
30	0.966	32.557	0.047	18.623
40	0.980	31.624	0.057	22.349
50	0.976	31.931	0.067	26.166
60	0.976	31.931	0.081	31.646
70	0.976	31.931	0.096	37.647
80	0.971	32.241	0.119	46.657
90	0.971	32.241	0.139	54.652
100	0.966	32.557	0.153	60.652
110	0.971	32.241	0.185	72.645
120	0.971	32.241	0.213	83.652
130	0.962	32.877	0.248	98.617
140	0.966	32.557	0.272	107.652
150	0.962	32.877	0.297	118.156
160	0.971	32.241	0.337	132.657
170	0.980	31.624	0.386	150.414
180	0.971	32.241	0.423	166.463
190	0.976	31.931	0.474	185.412
200	0.966	32.557	0.517	204.412

It can be seen that under different excitation voltages, the system damping ratio and total damping increase with the increase of excitation voltages, while the natural frequency and oscillation mass remain nearly constant.

Using the average values of f_n = 0.972, m_{osc} = 32.200 kg, the oscillation mass of oscillators with four different aspect ratios remains unchanged during the experiment. From Equations (5)–(7), it can be seen that the natural frequency, system damping ratio, and total damping of different oscillators are the same. Therefore, the experimental design is reasonable, and the experimental parameters are summarized in Table 3.

Table 3. Oscillation experimental parameters.

Name	Symbol [Unit]	Parameters
Width	D [m]	0.1
Length	l [m]	0.9
Oscillation mass	m_{osc} [Kg]	32.200
Stiffness	K [N/m]	1200
Natural frequency	f_n [Hz]	0.972
Range of velocity	U [m/s]	$0.680 \leq U \leq 1.214$
Reduced velocity	U_r	$7 \leq U_r \leq 12.5$
Reynolds number	$Re = \rho UD/\mu$	$59{,}441 \leq Re \leq 106{,}119$
Load resistance	R_L [Ω]	36

2.2.3. Error Analysis

This paper introduced the parameters: reduced velocity $U_r = U/f_n \times D$, amplitude ratio $A^* = A/D$, and frequency ratio $f^* = f_{osc}/f_{n,air}$, where f_{osc} is the main frequency of the system. In the experiment, a magnetic induction displacement transducer was used to measure the oscillator's real-time displacement. Its measurement range is 0–800 mm, the sensitivity is 0.1%, and the full-scale accuracy is ±0.05% (FS). The power output was calculated by collecting voltages of the load resistance in real-time. The measurement range is from −10 V to +10 V, and the full-scale accuracy is ±0.1% (FS).

All errors associated with the above parameters are caused by the experimental devices, the maximum error of A^* is less than ±0.004, the maximum error of P_{harn} is less than ±0.0026 W.

3. Flow-Induced Motion and Energy Harness

3.1. Flow-Induced Motion

The variation of amplitude ratio A^* and frequency ratio f^* with reduced velocity U_r for oscillators with four different aspect ratios (α = 1:1, α = 1.25:1, α = 1.5:1, α = 1.75:1) under different system damping ratios are illustrated in Figure 4.

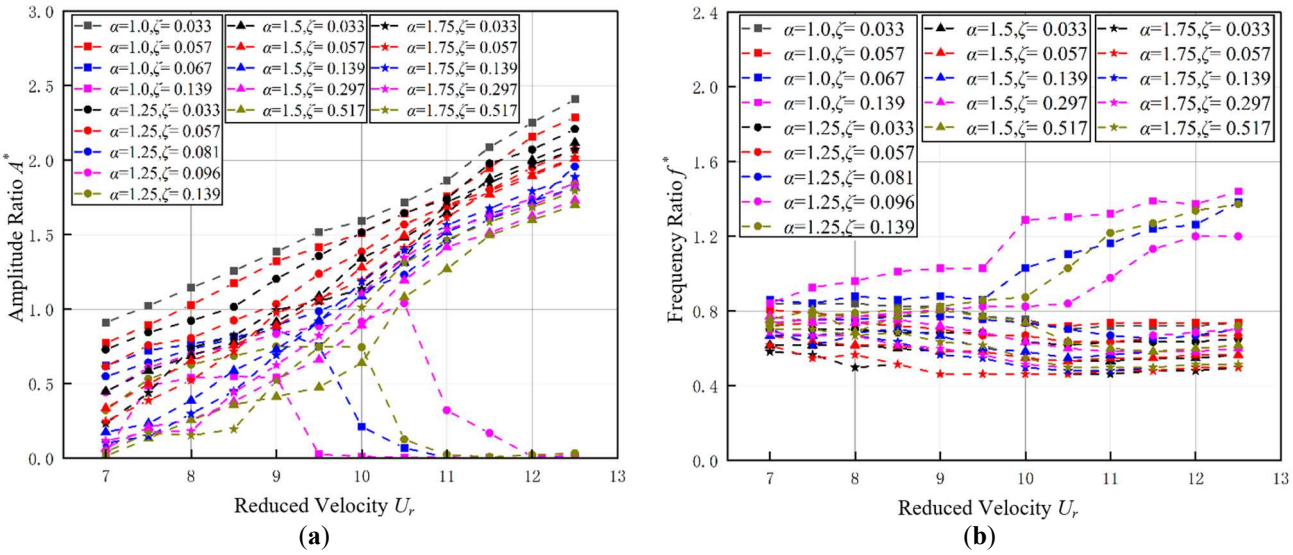

Figure 4. FIM of oscillators with different aspect ratios. (**a**) Amplitude ratio; (**b**) Frequency ratio.

According to Figure 4, it can be seen that under different system damping ratios, the CTAO will undergo the conversion of SG, HG to VIV. With the increase of the system damping ratio, the initial starting velocity of the oscillator will increase, and under the same working conditions, the oscillation intensity will gradually weaken.

(1) For the oscillator with α = 1:1, when $0.033 \leq \zeta \leq 0.057$, the oscillation mode is SG. As U_r increases: the oscillation mode gradually enters the VIV initial branch (VIV-I), the VIV-galloping transition branch and the galloping branch. During this process, A^* gradually increases, while f^* decreases slightly and stabilizes between 0.72 and 0.74; when $\zeta = 0.033$, $U_r = 12.5$, the maximum amplitude ratio $A^* = 2.408$; if the flow velocity continues to increase, A^* will continue to increase until the device is destroyed.

When $\zeta > 0.057$, the oscillation mode is VIV, As U_r increases: when $7 \le U_r \le 7.5$, A^* is very small and increases obviously with the increase of U_r, and the oscillation is characterized by the VIV-I; then the oscillation enters the VIV upper branch (VIV-U), and the larger the U_r, the larger the A^*, and the obvious locking phenomenon of f^* appears, which is stable between 0.9 and 1.03. In the locking interval, the range of U_r decreases from $7 \le U_r \le 9.5$ ($\zeta = 0.067$) to $7 \le U_r \le 9$ ($\zeta = 0.139$) with the increase of ζ; When $U_r > 9.5$, the oscillation enters the VIV down branch (VIV-D), A^* decreases, f^* increases with the increase of U_r and the oscillation becomes unstable.

(2) For the oscillator with α = 1.25:1, when $0.033 \le \zeta \le 0.081$, the oscillation mode is SG. As U_r increases: A^* gradually increases, while f^* decreases slightly and stabilizes between 0.63 and 0.67; when $\zeta = 0.034$, $U_r = 12.5$, the maximum amplitude ratio $A^* = 2.209$.

When $0.081 \le \zeta \le 0.139$, the oscillation mode is HG; as U_r increases: when $7 \le U_r \le 7.5$, A^* increases greatly, and the oscillation is characterized by the VIV-I; then the oscillation enters the VIV-U, the oscillation gradually strengthened, A^* increases, while f^* increases slightly and stabilizes between 0.8 and 0.85. In the locking interval, the range of U_r decreases from $7 \le U_r \le 10.5$ ($\zeta = 0.096$) to $7 \le U_r \le 10$ ($\zeta = 0.139$); when $U_r > 10.5$, A^* decreases significantly, and f^* increases significantly with the increase of U_r, it indicates that the oscillation enters the VIV-D. At this time, there is a critical velocity (CV), that is, when the flow velocity exceeds CV, the oscillation can be excited by the external excitation into the galloping, and the CV increases from $U_r = 11.5$ ($\zeta = 0.096$) to $U_r = 12.5$ ($\zeta = 0.139$), it indicates that the ability of the system to convert VIV into galloping through external excitation is weakened. When the oscillation mode is HG, f^* is stable between 0.67 and 0.72, when $\zeta = 0.096$, $U_r = 12.5$, the maximum amplitude ratio of HG can reach $A^* = 1.845$.

When $\zeta > 0.139$, the oscillation mode is VIV.

(3) For the oscillator with α = 1.5:1, in the whole range of $0.033 \le \zeta \le 0.517$, the oscillation mode is SG. As U_r increases, A^* increases gradually, f^* is stable between 0.53 and 0.6; when $\zeta = 0.033$, $U_r = 12.5$, the maximum amplitude ratio $A^* = 2.116$.

The detailed analysis reveals that when $\zeta = 0.0517$, the oscillation becomes unstable: when $9 \le U_r \le 10$, the increase of A^* slows down, while f^* continues to rise; as the flow velocity increases further, A^* increases, and f^* decreases, and the oscillation shows the characteristics of galloping. According to Reference [30], this indicates that the damping ratio of the critical galloping (CG) of the oscillator with α = 1.5:1 is close to $\zeta = 0.0517$, and the ability of self-excited galloping is weak at $\zeta = 0.0517$.

（4）For the oscillator with α = 1.75:1, in the whole range of $0.033 \le \zeta \le 0.517$, the oscillation mode is SG. As U_r increases: A^* increases gradually, f^* is stable between 0.46 and 0.52; when $\zeta = 0.033$, $U_r = 12.5$, the maximum amplitude ratio $A^* = 2.070$.

It is evident that the oscillator with α = 1.75:1 has no oscillation instability, that is, the oscillator with α = 1.75:1 has better oscillation performance than the oscillator with α = 1.5:1.

3.2. Energy Harness

From Equations (2) and (3), it can be seen that the power output P_{harn} and the efficiency η_{harn} are positively correlated with A, f_{osc} and V_B, and η_{harn} is negatively correlated with U. Therefore, A^*, f^*, U_r and ζ will directly affect the size of P_{harn} and η_{harn}. In the experiment, P_{harn} can also be obtained by the following expression：

$$P_{harn} = \frac{1}{T_{osc}} \int_0^{T_{osc}} \frac{u^2(t)}{R_L} dt \tag{8}$$

where T_{osc} is the oscillation period; $u(t)$ is the collected instantaneous voltage.

Figure 5 shows the variation of power output P_{harn} and the efficiency η_{harn} with reduced velocity under different system damping ratios of four oscillators with different aspect ratios of α = 1:1, α = 1.25:1, α = 1.5:1 and α = 1.75:1.

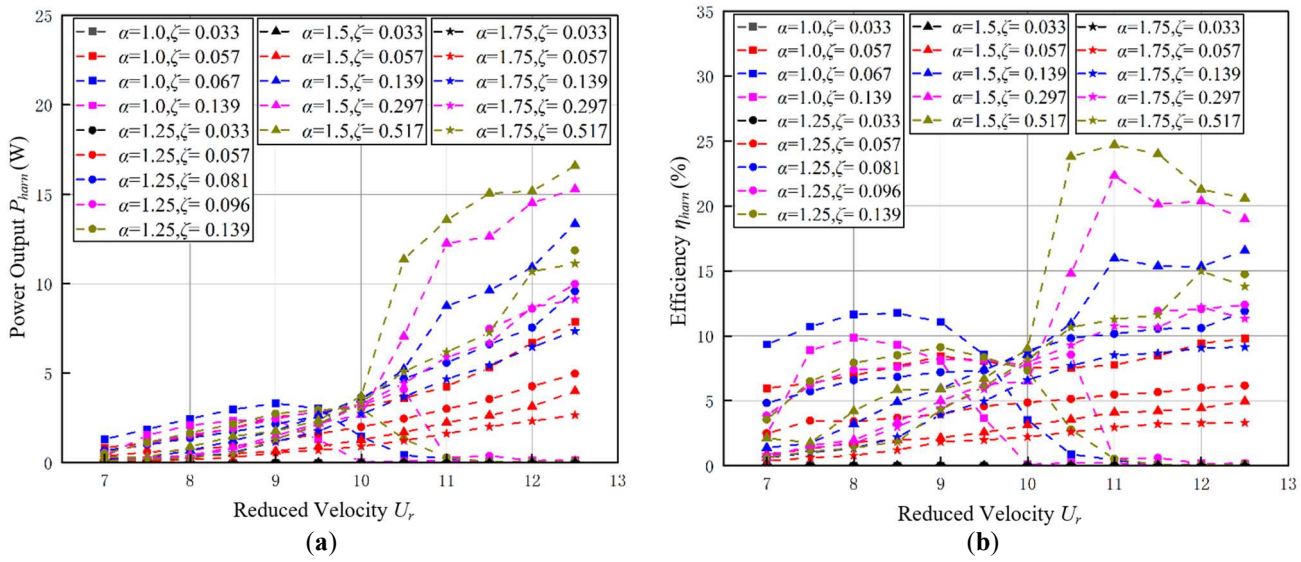

Figure 5. Energy harness of an oscillator with different aspect ratios. (**a**) Power output; (**b**) Efficiency.

According to Section 3.1 and Figure 5:

(1) For the oscillator with α = 1:1, when 0.033 ≤ ζ ≤ 0.057, the oscillation mode is SG. As U_r increases: P_{harn} continues to rise because η_{harn} is negatively correlated with U^3. It increases first and then tends to be stable. When ζ = 0.033, the corresponding V_B = 0 V, and the power generation damping is very small, so P_{harn} and η_{harn} are close to 0; when ζ = 0.057, with the increase of ζ, the oscillation is weakened, but the increase of power generation damping is much higher than the decrease of A^*, and the oscillation frequency is not much different, so ζ = 0.057 compared with ζ = 0.033, P_{harn} and η_{harn} increase significantly; when ζ = 0.057, U_r = 12.5, the maximum power output P_{harn} = 7.870 W.

When ζ > 0.057, the oscillation mode is VIV. As U_r increases: in the VIV-I and VIV-U, P_{harn} and η_{harn} increase; while entering the VIV-D, P_{harn} and η_{harn} decreased rapidly to 0. Similarly, due to the negative correlation between η_{harn} and U^3, P_w dominates the change of η_{harn} at high flow velocity, so the optimal efficiency does not always appear in the galloping; when ζ =0.067, U_r = 8.5, the optimal efficiency η_{harn} = 11.763%.

(2) For the oscillator with α = 1.25:1, when 0.033 ≤ ζ ≤ 0.081, the oscillation mode is SG. As U_r increases: P_{harn} increases monotonically, η_{harn} increases first and then decreases slightly; with the increase of ζ, P_{harn} and η_{harn} increased significantly.

When 0.081 ≤ ζ ≤ 0.139, the oscillation shows the characteristics of HG as U_r increases: in the VIV-I and VIV-U, P_{harn} and η_{harn} increase; while entering the VIV-D, P_{harn} and η_{harn} decreased rapidly to 0; when the flow velocity exceeds CV and the oscillation enters the galloping through external excitation, both of them increase significantly, P_{harn} increases, and η_{harn} increases first and then tends to be stable; when ζ = 0.139, U_r = 12.5, the maximum power output P_{harn} = 11.874 W and the optimal efficiency η_{harn} =14.745%.

When ζ > 0139, the oscillation mode is VIV. As U_r increases: both P_{harn} and η_{harn} increased first and then decreased.

(3) For the oscillator with α = 1.5:1, the whole range of 0.033 ≤ ζ ≤ 0.517, the oscillation mode is SG. As U_r increases: P_{harn} monotonically increases; when 0.033 ≤ ζ ≤ 0.139, η_{harn} increases first and then stabilizes, and with the increase of ζ, both of them rise significantly; when 0.139 ≤ ζ ≤ 0.517, η_{harn} increases first and then decreases, while the growth rates of both parameters diminish as ζ increases. This is because ζ has a great influence on the amplitude A^* at this time. The decrease of A^* is only slightly smaller than the increase of power generation damping, and the oscillation frequency is still not much different. Therefore, the increase of P_{harn} and η_{harn}. When ζ =0.517, U_r =12.5, the maximum power output P_{harn} =16.588 W; when ζ = 0.517, U_r = 11.5, the optimal efficiency η_{harn} = 24.706%.

(4) For the oscillator with α = 1.75:1, in the whole range of 0.033 ≤ ζ ≤ 0.517, the oscillation mode is SG. As U_r increases: The variation trend of P_{harn} and η_{harn} is the same as that of the oscillator with α = 1.5:1. When ζ = 0.517, U_r = 11.5, the maximum power output P_{harn} = 11.125 W; when ζ = 0.517, U_r = 12, the optimal efficiency η_{harn} = 15.000%.

4. Wake Structures

Referring to the wake mode summarized by Williamson et al. [31,32], the selected flow field data with a representative period are analyzed after repeated experiments and PIV measurements. It is found that the higher the flow velocity is, the more obvious the vortex in the PIV cloud image is, and the less the messy velocity vector is. Combined with the results of Section 3.1, it can be seen that the oscillation modes of four different forms of oscillators

are SG when the system damping ratio $\zeta = 0.055$. Therefore, the experiment is carried out under the conditions of $\zeta = 0.055$ and $U_r = 12$, aiming to eliminate other factors and better reflect the influence of the aspect ratio. The experimental parameters of the PIV system are shown in Table 4.

Table 4. Experimental parameters of PIV system.

Name	Parameters
Reduced velocity (U_r)	12
Velocity	1.266 m/s
Re	110664
Exposure time (Δt)	1700 μs
Shooting frequency of the double PIV images	4.456 Hz
The method of processing the double PIV images	Vector interpolation

(1) The wake of the oscillator with α = 1:1 in an oscillation period is shown in Figure 6. In the figure, the wake vortex forms, develops and falls off from the surface of the upper and lower plates of the oscillator. The black solid line is the position of the oscillator at the corresponding time, and the reverse vortex is formed on the upper surface, which is recorded as F1, F2, F3…; the positive vortex is formed on the lower surface, recorded as Z1, Z2, Z3…. The same is true for the subsequent wake structure.

It can be seen that in an oscillation period, the wake mode is 4P, that is, as the oscillator vibrates up and down, the wake appears as four pairs of vortices in both positive and negative directions.

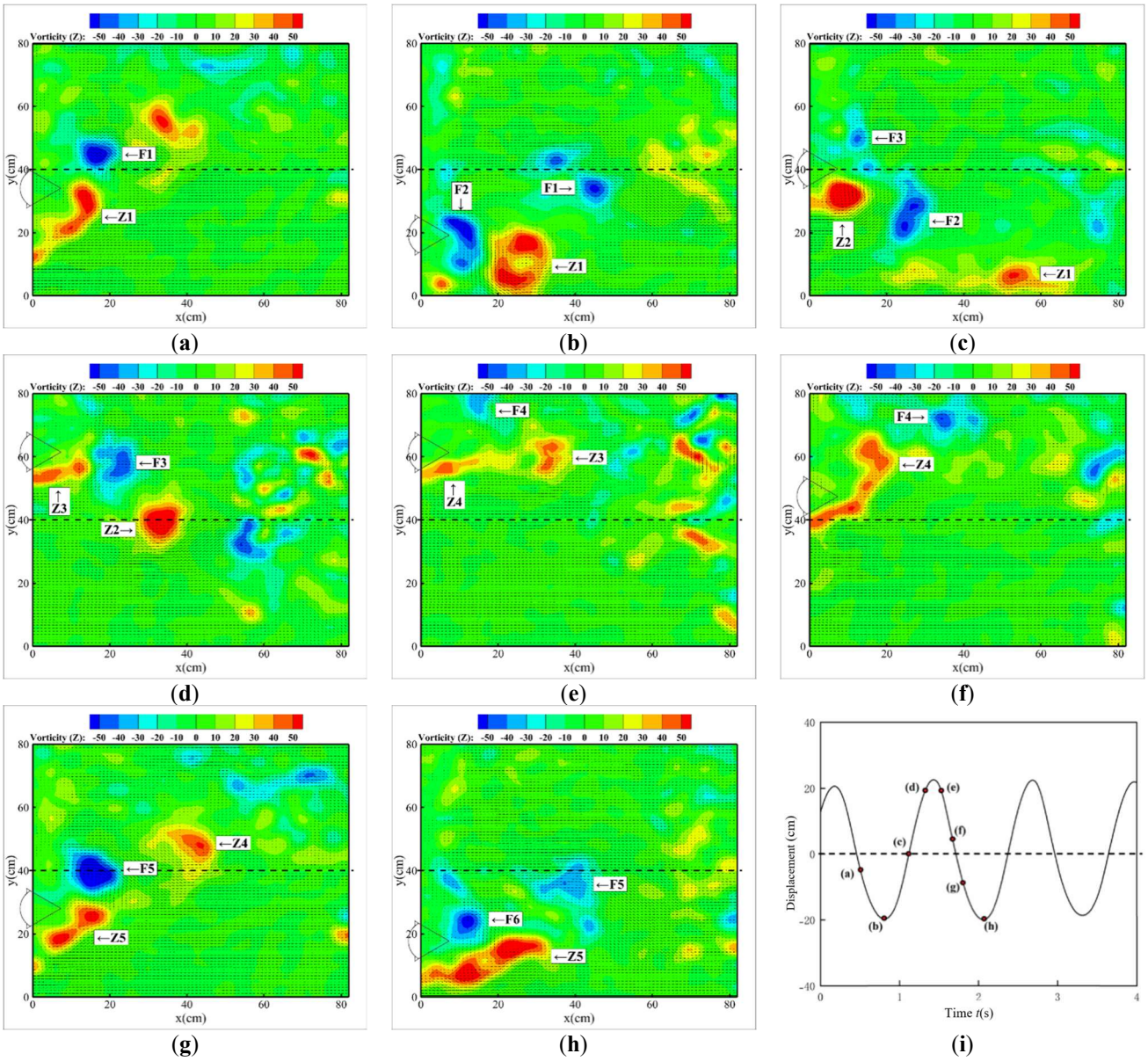

Figure 6. The wake structures of the oscillator with α = 1:1. (**a**–**h**) Instantaneous wake structures; (**i**) Displacement time history.

(2) The wake of the oscillator with α = 1.25:1 in an oscillation period is shown in Figure 7. The wake mode is 3P, that is, in an oscillation period, as the oscillator vibrates up and down, the wake appears as three pairs of vortices in both positive and negative directions and becomes more broken.

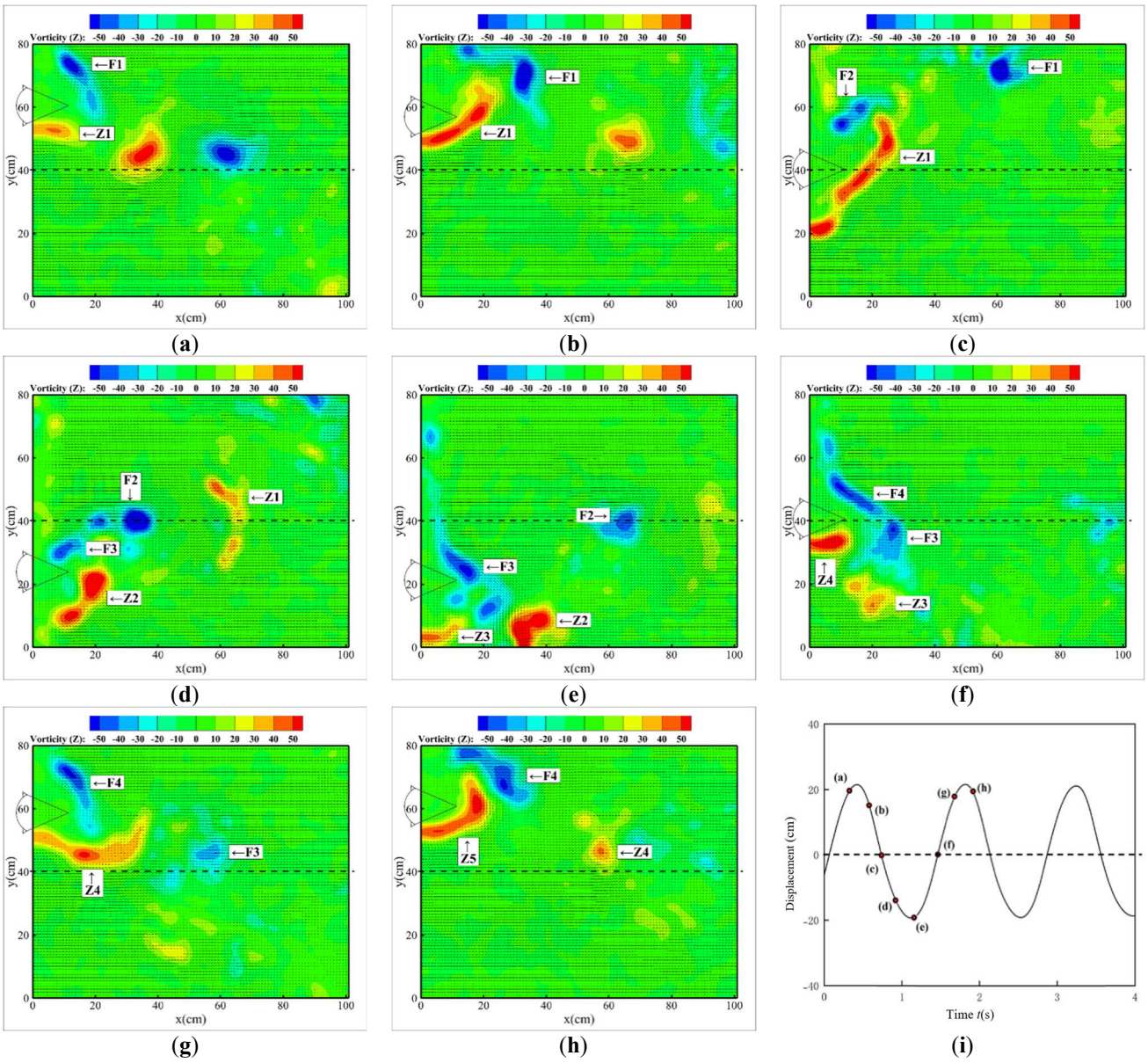

Figure 7. The wake structures of the oscillator with α = 1.25:1. (**a**–**h**) Instantaneous wake structures; (**i**) Displacement time history.

(3) The wake of the oscillator with α = 1.5:1 in an oscillation period is shown in Figure 8. The wake mode is 3P, that is, in an oscillation period, as the oscillator vibrates up and down, the wake appears as three pairs of vortices in both positive and negative directions, and the scale becomes larger.

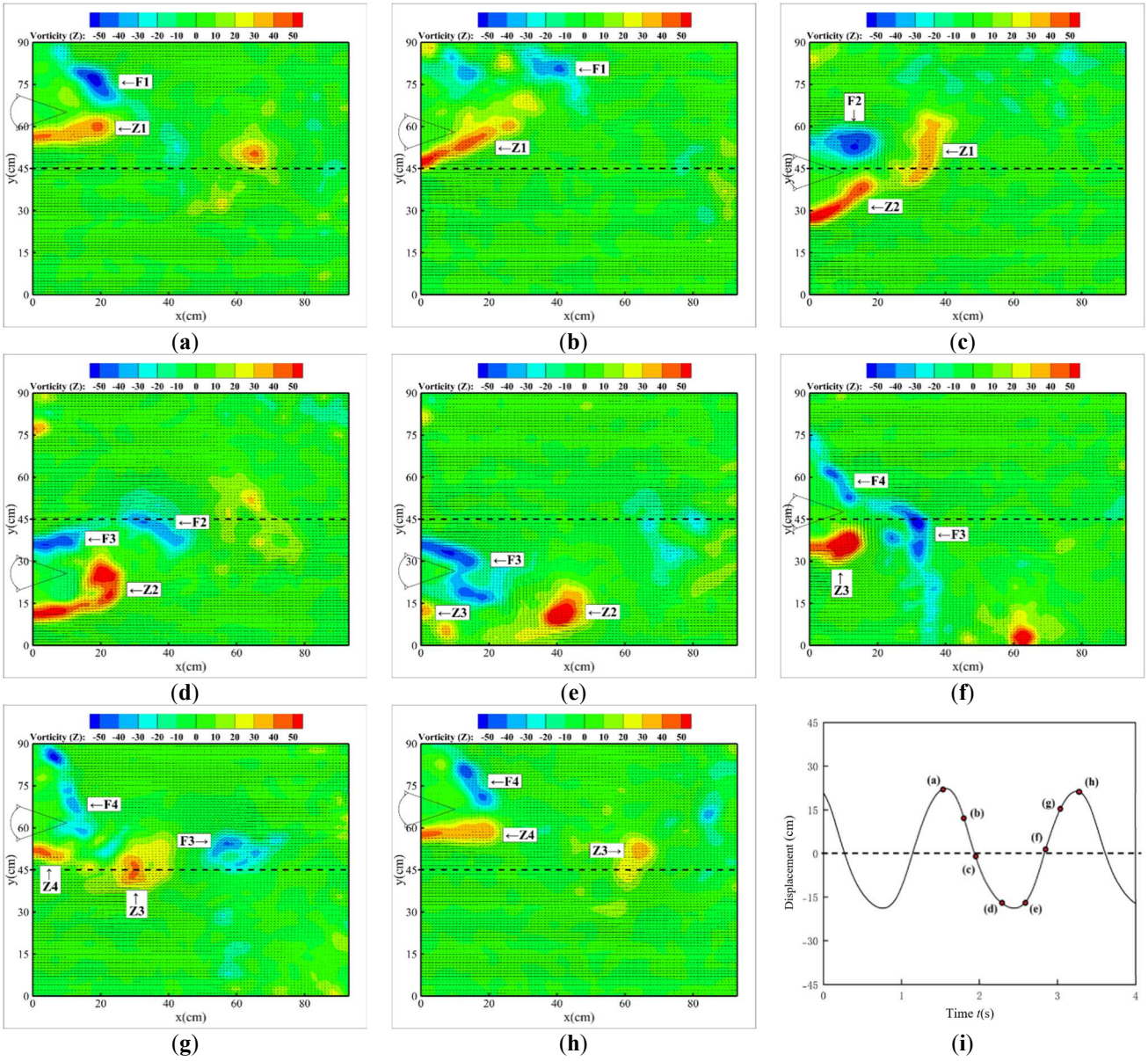

Figure 8. The wake structures of the oscillator with α = 1.5:1. (**a–h**) Instantaneous wake structures; (**i**) Displacement time history.

(4) The wake of the oscillator with α = 1.75:1 in an oscillation period is shown in Figure 9. The wake mode is 3P, that is, in an oscillation period, as the oscillator vibrates up and down, the wake appears as three pairs of vortices in both positive and negative directions. The time for vortex growth, development, and final shedding becomes longer, and the time for the development and shedding of positive vortices is longer than that of reverse vortices, resulting in a pressure difference and a longer oscillation period.

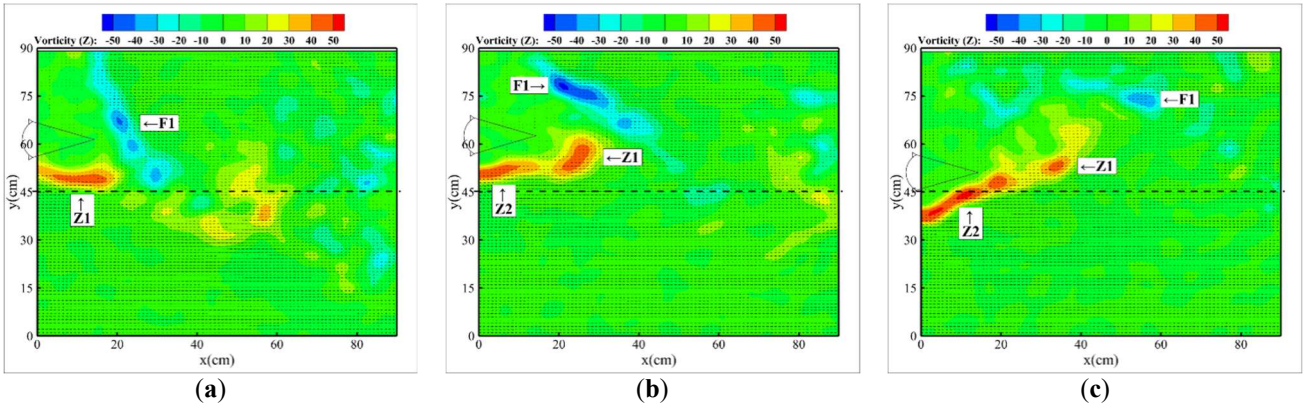

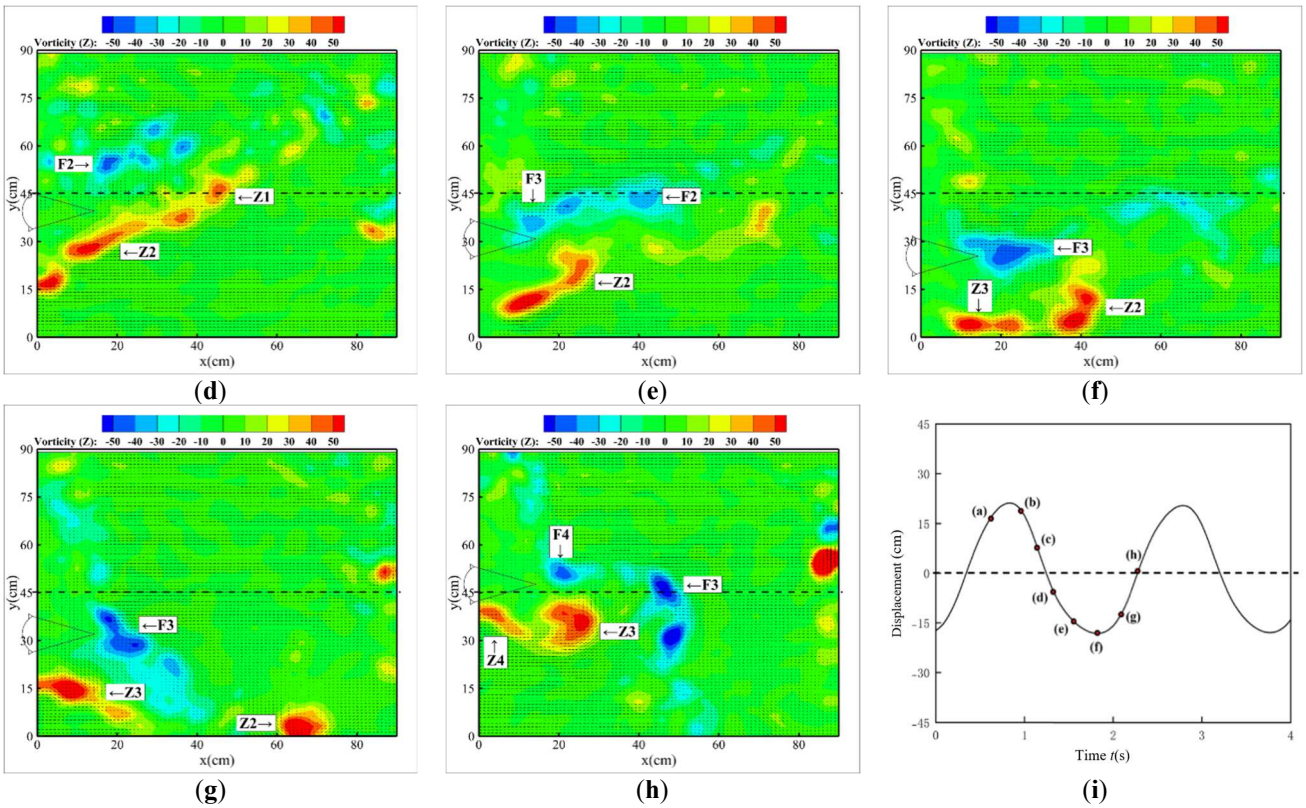

Figure 9. The wake structures of the oscillator with α = 1.75:1. (**a**–**h**) Instantaneous wake structures; (**i**) Displacement time history.

In the SG, the summary of the wake structures is shown in Table 5 when the reduced velocity is 12.

Table 5. Summary of wake structures.

	α = 1:1	α = 1.25:1	α = 1.5:1	α = 1.75:1
Reduced velocity	12	12	12	12
Oscillation mode	SG	SG	SG	SG
Wake mode	4P	3P	3P	3P
Image description	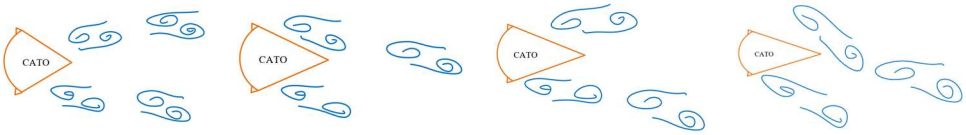			

It is evident that the oscillator with a small aspect ratio produces more vortex shedding. At the same reduced velocity, the wake modes of the four forms of oscillators are similar, and the oscillation is very stable.

5. Conclusions

This paper focused on the flow-induced motion (FIM) and energy harness of CTAO. Additionally, PIV was introduced to capture the wake at different reduced velocity, in order to analyze the wake structures. The FIM, energy harness and wake structures of the CTAO under different working conditions were systematically summarized, which provides theoretical and data support for the optimal oscillators of flow-induced motion tidal energy conversion system.

(1) Oscillation response: As the system damping ratio increases, the initial starting flow velocity of the CTAO rises, the oscillation intensity is weakened, and the oscillation mode changes from SG and HG to VIV. Conversely, as the aspect ratio increases, the system damping ratio and the reduced velocity range for galloping are expanded, that is, the ability of oscillators to gallop under self-excitation or external excitation is enhanced. Moreover, both the maximum amplitude ratio and the frequency ratio decrease under the same other conditions. When $\zeta = 0.033$, U_r = 12.5, the maximum amplitude ratio $A^* = 2.408$ for oscillators with α = 1:1. In the galloping, the frequency ratio f^* decreases from about 0.73 at α = 1:1 to about 0.5 at α = 1.75:1.

(2) Optimization of energy harness: When the oscillation is in the same mode and system damping ratio, the power output and the efficiency decrease with the increase of the aspect ratios. However, appropriately increasing the

aspect ratio benefits the energy utilization and conversion of the system. The maximum power output P_{harn} = 16.588 W and the optimal efficiency η_{harn} = 24.706% appear in oscillators with α = 1.5:1.

(3) Wake structures: In the SG, the wake mode is not much different, which is 4P or 3P, which means the oscillation is very stable. As the aspect ratio increases: the wake vortex is more broken and its scale increases. However, the force area of oscillators becomes larger, and the vortex attachment phenomenon is more obvious, so the force effect of oscillators is better, and the oscillation is more stable. At the same time, the time for vortex growth, development, and final shedding becomes longer, and the time for the development and shedding of positive vortices is longer than that of reverse vortices, resulting in a pressure difference and a longer oscillation period.

Acknowledgments

Results were obtained from State Key Laboratory of Hydraulic Engineering Intelligent Construction and Operation of Tianjin University.

Author Contributions

Conceptualization, X.Y. (Xiang Yan); Methodology, X.Y. (Xiang Yan); Software, J.X.; Validation, L.J.; Formal Analysis, X.Y. (Xu Yang) and S.N.; Investigation, L.J.; Resources, X.G. and X.Y. (Xiang Yan); Data Curation, X.Y. (Xu Yang) and Y.Y.; Writing—Original Draft Preparation, L.J.; Writing—Review & Editing, X.Y. (Xu Yang), Y.Y., X.G. and X.Y. (Xiang Yan); Visualization, L.J. and J.X.; Supervision, Y.Y. and X.Y. (Xiang Yan); Project Administration, Y.Y. and X.G.; Funding Acquisition, X.Y. (Xu Yang), X.Y. (Xiang Yan) and N.S.

Ethics Statement

Not applicable.

Informed Consent Statement

Not applicable.

Funding

The research was founded by National Key R&D Program of China (Grant No. 2022YFB4200702), Tianjin Science and Technology Plan Project (Grant No. 23ZYQYGX00140), National Natural Science Foundation of China (Grant No. 52409085), the Science and Technology Project of Hebei Education Department (Grant No. BJK2023099) and the Hebei Natural Science Foundation (Grant No. E2022402074).

Declaration of Competing Interest

The authors declare that they have no known competing financial interests or personal relationships that could have appeared to influence the work reported in this paper.

References

1. Wang C, Zhang Y, Deng Z. Wave power extraction for an oscillating water column device consisting of a surging front and back lip-wall: an analytical study. *Renew. Energy* **2022**, *184*, 100–114.
2. Su X, Wang X, Xu W, Yuan L, Xiong C, Chen J. Offshore Wind Power: Progress of the Edge Tool, Which Can Promote Sustainable Energy Development. *Sustainability* **2024**, *16*, 7810.
3. Rusu EVC. Harvesting Offshore Renewable Energy an Important Challenge for the European Coastal Environment. *Sustain. Mar. Struct.* **2023**, *5*, 11–13.
4. Lian J, Cui L, Fu Q. Offshore Renewable Energy Advance. *Mar. Energy Res.* **2024**, *1*, 10006.
5. Neshat M, Mirjalili S, Sergiienko NY, Esmaeilzadeh S, Amini E, Heydari A, et al. Layout optimisation of offshore wave energy converters using a novel multi-swarm cooperative algorithm with backtracking strategy: A case study from coasts of Australia. *Energy* **2022**, *239*, 122463.
6. Yang L, HAAS KA, FRITZ HM. Theoretical Assessment of Ocean Current Energy Potential for the Gulf Stream System. *Mar. Technol. Soc. J.* 2013, 47, 101–112.
7. Bernitsas MM. Harvesting energy by flow included motions. In *Springer Handbook of Ocean Engineering*, 1st ed.; Dhanak MR, Xiros NI, Eds.; Springer: Cham, Switzerland, 2016; pp. 1163–1244.

8. HAAS K. *Assessment of Energy Production Potential from Ocean Currents Along the United States Coastline (Report No. DOE/EE/2661-10)*; Georgia Institute of Technology: Atlanta, GA, USA, 2013.
9. Williamson CHK, Govardhan R. Vortex-Induced Vibrations. *Annu. Rev. Fluid Mech.* **2004**, *36*, 413–455.
10. Sarpkaya T. A Critical Review of the Intrinsic Nature of Vortex-Induced Vibrations. *J. Fluids Struct.* **2004**, *19*, 389–447.
11. Bearman PW. Circular Cylinder Wakes and Vortex-Induced Vibrations. *J. Fluids Struct.* **2010**, *27*, 648–658.
12. Lekkala MR, Mohamed L, Hafiz MFU, Kim, DK. A practical technique for hydrodynamic coefficients modification in SHEAR7 for fatigue assessment of riser buoyancy modules under vortex-induced vibration. *Ocean Eng.* **2020**, *217*, 107760.
13. Lekkala MR, Latheef M, Jung JH, Coraddu A, Zhu H, Srinil N, et al. Recent advances in understanding the flow over bluff bodies with different geometries at moderate Reynolds numbers. *Ocean Eng.* **2022**, *261*, 111611.
14. Wang J, Geng L, Ding L, Zhu H, Yurchenko D. The state-of-the-art review on energy harvesting from flow-induced vibrations. *Appl. Energy*. **2020**, *267*, 114902.
15. Wang J, Sun S, Tang L, Hu G, Liang J. On the use of metasurface for Vortex-Induced vibration suppression or energy harvesting. *Energy Convers. Manag.* **2021**, *235*, 113991.
16. Zhu H, Tang T, Gao Y, Zhou T, Wang J. Flow-induced vibration of a trapezoidal cylinder placed at typical flow orientations. *J. Fluids Struct.* **2021**, *103*, 103291.
17. Bernitsas MM, Raghavan K, Ben-Simon Y, Garcia EMH. VIVACE (Vortex Induced Vibration Aquatic Clean Energy): A new concept in generation of clean and renewable energy from fluid flow. *J. Offshore Mech. Arct. Eng.* **2008**, *130*, 041101.
18. Bernitsas MM, Ben-Simon Y, Raghavan K, Garcia EMH. The VIVACE converter: model tests at high damping and Reynolds number around 105. *J. Offshore Mech. Arct. Eng.* **2009**, *131*, 011102.
19. Park H, Kumar R, Bernitsas MM. Enhancement of flow-induced motion of rigid circular cylinder on springs by localized surface roughness at $3.0 \times 10^4 \leq Re \leq 1.2 \times 10^5$. *Ocean Eng*. **2013**, *72*, 403–415.
20. Chen Z, Alam MM, Qin B, Zhou Y. Energy harvesting from and vibration response of different diameter cylinders. *Appl. Energy* **2020**, *278*, 115737.
21. Feng W, Yang X, Yan X, Li L. Investigation on Flow-Induced Rotation of Coupled Double Cylinders Arranged in Tandem. In Proceedings of the ASME 2024 43rd International Conference on Ocean, Offshore and Arctic Engineering, Singapore, 9–14 June 2024.
22. Zhang J, Liu F, Lian J, Yan X, Ren Q. Flow Induced Vibration and Energy Extraction of Equilateral Triangle Prism at Different System Damping Ratios. *Energies* **2016**, *9*, 938.
23. Yan X, Lian J, Liu F, Ren Q, Zhang J, Shao N. Experimental investigation on the galloping characteristics of the T-section prism. *J. Vib. Eng.* **2019**, *32*, 431–438. (In Chinese)
24. Lian J, Wu Z, Yao S, Yan X, Wang X, Jia Z, et al. Experimental Investigation of Flow-Induced Motion and Energy Conversion for Two Rigidly Coupled Triangular Prisms Arranged in Tandem. *Energies* **2022**, *15*, 8190.
25. Ran D, Lian J, Yan X, Liu F, Shao N, Yang X, et al. Flow-Induced Motion and Energy Conversion of the Cir-T-Att Oscillator in a Flow Field with a High Reynolds Number. *J. Mar. Sci. Eng.* **2023**, *11*, 795.
26. Liu F, Xiang J, Yan X, Feng W, Shao N, Wang X. Experimental study on the flow-induced motion of a "circle-triangle-attachment" combined section oscillator. *J. Vib. Shock* **2025**, *44*, 55–64. (In Chinese)
27. Yan X, Lian J, Liu F, Wang X, Shao N. Hydrokinetic energy harness of Flow-induced motion for triangular prism by varying magnetic flux density of generator. *Energy Convers. Manag.* **2021**, *227*, 113553.
28. Shao N, Lian J, Liu F, Yan X, Li P. Experimental investigation of flow induced motion and energy conversion for triangular prism. *Energy* **2020**, *194*, 116865.
29. Lian J, Ran D, Yan X, Liu F, Shao N, Wang X, et al. Hydrokinetic energy harvesting from flow-induced motion of oscillators with different combined sections. *Energy* **2023**, *269*, 126814.
30. Lian J, Yan X, Liu F, Zhang J, Ren Q, Yang X. Experimental investigation on soft galloping and hard galloping of triangular prisms. *Appl. Sci.* **2017**, *198*, 1–27.
31. Williamson CHK, Roshko A. Vortex formation in the wake of an oscillating cylinder. *J. Fluids Struct.* **1988**, *2*, 355–381.
32. Williamson CHK, Jauvtis N. A high-amplitude 2T Mode of vortex-induced vibration for a light body in XY motion. *Eur. J. Mech. B/Fluids* **2004**, *23*, 107–114.